International Symposium
On Turbulence and Shear Flow
Phenomena (TSFP-8)
August 28 - 30, 2013 Poitiers, France

COHERENCE AND REYNOLDS STRESSES IN THE TURBULENT WAKE BEHIND A CURVED CIRCULAR CYLINDER

José P. Gallardo, Bjørnar Pettersen
Department of Marine Technology
Norwegian University of Science and Technology
NO-7491 Trondheim, Norway
jose.p.gallardo@ntnu.no

Helge I. Andersson
Department of Energy and Process Engineering
Norwegian University of Science and Technology
NO-7491 Trondheim, Norway

ABSTRACT

The turbulent wake behind a curved circular cylinder is investigated based on data from a direct numerical simulation. A second-order finite-volume solver with an immersed boundary method was used to solve the incompressible Navier–Stokes equations. In this paper we analyse the instantaneous vortical structures, the proper orthogonal decomposition (POD) of the flow, and relevant Reynolds stress components. Despite the complexity of the instantaneous vortical structures, the wake dynamics are governed by the quasi-periodic shedding of primary vortices. Between 24% and 50% of the kinetic energy in the POD is captured by the two most energetic modes, and about 200 modes are needed to capture 90% of the kinetic energy. These findings suggest that the present case is suited for a low-dimensional representation. The magnitude of the Reynolds stresses varied considerably depending on the depth at which they where sampled. This dependence is likely related to the strength of the vortex shedding and the intensity of the secondary flows induced by the curvature of the cylinder. As a consequence of the combination of these two effects, the correlation between streamwise and vertical velocity fluctuations is highest at around half the depth of the curved cylinder.

INTRODUCTION AND MOTIVATION

When a uniform circular cylinder loses its two-dimensionality either by truncation (Frederich & Thiele, 2011), tapering (Narasimhamurthy *et al.*, 2009), tilting (Zhou *et al.*, 2010), bending (Miliou *et al.*, 2007), or a combination of these modifications, the wake it creates when it encounters an incoming flow becomes highly complex and three-dimensional. The study of these three-dimensional bluff-body configurations is important because they frequently appear in engineering applications. For instance, catenary risers are commonly used in marine operations to convey fluids from the seabed. Their interaction with sea currents creates wakes which may transport pollutants in case of leakages, or interact with nearby structures.

In order to study the dynamics of the flow past a catenary riser, Miliou *et al.* (2007) approximated this bluff body geometry by a quarter segment of a ring. They conducted numerical simulations at laminar and transitional Reynolds numbers of 100 and 500, respectively; two opposite inflow velocity directions were considered, both aligned with the plane of curvature of the ring. In the case in which the inflow was directed towards the external face of the quarter-of-ring the resulting wake topology consisted of a staggered array of vortices along most of the span of the cylinder. Although the vortex shedding dominated the periodicity of the flow dynamics in this case, the drag coefficients and the pressures at the stagnation and base line exhibited significant variations along the curved span of the cylinder. The second flow configuration studied, in which the incoming flow was directed towards the inner-face of the quarter-of-ring, exhibited suppression of the vortex shedding. This was attributed to the strong axial flows induced by the curvature of the cylinder.

Although straight cylinders at a constant inclination angle with respect to the incoming flow direction have been previously studied experimentally and numerically (see e.g. Ramberg, 1983; Zhou *et al.*, 2010) and are relatively well documented, the effect of gradual inclination of the axis in the curved cylinder case deserves further study. An interesting extension of this case was the study of the laminar flow past the same curved cylinder under forced cross-flow vibrations by De Vecchi *et al.* (2009).

Our approach in the present investigation is to study the flow past the same geometry as that used by Miliou *et al.* (2007) and De Vecchi *et al.* (2009), but at a higher Reynolds number corresponding to the sub-critical regime; this produces a turbulent wake and instability in the free shear layers. The convex flow configuration, i.e. with the flow directed towards the external face of the quarter-of-ring, was chosen for the study of the shedding dynamics and the coherence in the wake. The methodology used for this purpose is direct numerical simulation (DNS). Our objectives

are to characterize the effects of curvature in the coherence of the wake and in relevant components of the Reynolds stress tensor. In order to accomplish this, we focused on the analysis of the instantaneous vortical structures, the proper orthogonal decomposition (POD) of the flow, and relevant second-order statistics.

FLOW CONFIGURATION AND NUMERICAL METHODOLOGY

The flow configuration used in the present investigation was adapted from that used by Miliou *et al.* (2007). The bluff-body geometry consists of a quarter of ring with radius $R = 12.5D$, where D is the cross-sectional diameter of the cylinder. Both free-ends of the quarter-of-ring were extended, by $L_v = 6D$ in the vertical direction, and $L_h = 10D$ in the horizontal direction. The free-stream velocity U_∞ is directed towards the outer face of the ring, as depicted by figure 1.

The flow field is obtained from the direct numerical solution of the incompressible Navier–Stokes equations, which is computed with the second-order finite volume code MGLET (Manhart, 2004). This solver uses a staggered Cartesian grid with non-equidistant spacing, and integration in time is done explicitly by a third-order Runge–Kutta scheme. Representation of complex geometries is done with an immersed boundary method (IBM) algorithm; details of this IBM and its validation are found in Peller *et al.* (2006).

For the simulations, the Reynolds number based on the cross-sectional diameter D and free-stream velocity U_∞, is set at 3900. In order to check the spatial resolution, we conducted simulations on a straight cylinder at the same Re, as well as two simulations using the curved cylinder. The results presented in this paper were obtained from the simulations conducted on a $N_x \times N_y \times N_z$=2160×860×800 mesh, resulting in about 1.47×10^9 grid cells. This resolution was adequate to resolve all the relevant scales in the boundary layers as well as in the wake. Concerning boundary conditions, we used the following:

- uniform velocity U_∞ at the inflow plane;
- a Neumann condition for the velocity together with the pressure set to zero, resulting in a zero stress condition at the outflow plane;
- free-slip conditions at the side, top and bottom planes.

A time of $750U_\infty/D$ was needed to eliminate the initial transients, after which statistics were sampled for $1200U_\infty/D$. Additionally, two-dimensional snapshots in (x,y)- and (y,z)-planes were gathered for a period of $100U_\infty/D$.

RESULTS AND DISCUSSION

In order to obtain a general impression of the wake behind this particular bluff-body configuration, the wake topology represented by instantaneous vortical structures is presented first. Then, results from the POD of the flow field are used to identify the dominant flow features. Finally, relevant Reynolds stresses at different depths are presented and discussed.

Instantaneous wake topology

Figure 2 shows a three-dimensional snapshot of the instantaneous wake topology represented by iso-surfaces of

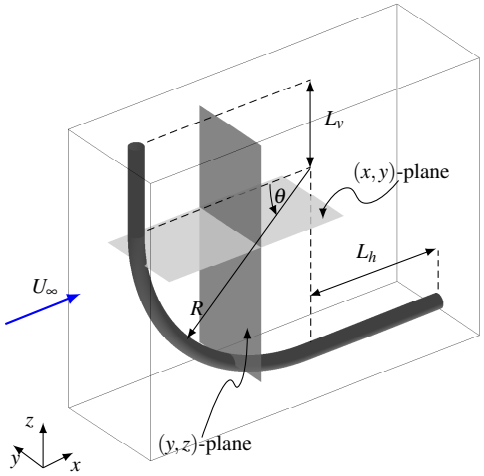

Figure 1. Flow configuration depicting the curved cylinder which consists of a quarter-of-ring with radius R, and horizontal and vertical extensions with lengths L_h and L_v, respectively. The origin in the (x,y)-plane coincides with the axis of the straight extension; the upper (x,y)-plane is located at $z = 24D$, and the curved-straight interface at $z = 18D$.

λ_2 (Jeong & Hussain, 1995). Additionally, slices of enstrophy $|\omega|^2$ at different representative planes normal to the three Cartesian directions are used to visualize shear layers.

Although the instantaneous wake topology in figure 2(c) is apparently highly complex and disordered, the periodic shedding of primary Kármán vortices is an important contribution to the coherence of the flow field. This process is depicted by figure 2(a), which shows the rolling-up of the shear layers detached from the walls of the curved cylinder leading to the formation of primary vortices. The axes of these primary vortices are partially aligned with the curved axis of the cylinder, as figure 2(c) depicts. Behind the lower part of the curved cylinder (figure 2.b) the wake becomes less organized. Here the shear layers are highly unstable, and the formation of primary vortices seems to be suppressed.

Small structures convected downstream by the main vortices is the signature of the turbulent flow in this case. These structures range widely in size and orientation, in comparison with the secondary structures observed in the transitional state to turbulence of the wake behind a straight circular cylinder (Williamson, 1996*a*).

Proper orthogonal decomposition

Proper orthogonal decomposition (POD) of the flow field is used to analyse the coherence and dominant dynamics in the wake behind the curved cylinder. In this method, the flow field $\mathbf{u}(\mathbf{x},t)$ is decomposed into spatial orthogonal modes ϕ_m, and corresponding temporal modes $a_m(t)$,

$$\mathbf{u}(\mathbf{x},t) = \mathbf{u}_0(\mathbf{x}) + \sum_{m=1}^{M} a_m(t)\phi_m(\mathbf{x}), \qquad (1)$$

where $\mathbf{u}_0$ is the steady base flow. The set of orthogonal modes ϕ_m and a_m is optimal in terms of representing the energy of the velocity field (Berkooz *et al.*, 1993).

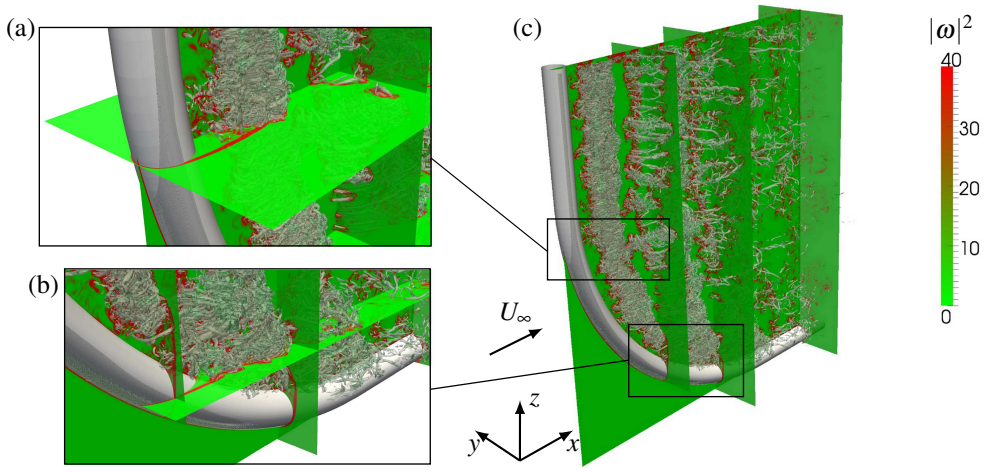

Figure 2. Instantaneous wake topology represented by iso-surfaces of $\lambda_2 = -25$ plotted together with slices of enstrophy $|\omega|^2$ in (x,y)-, (y,z)-, and (x,z)-planes. Differences in the near wake are depicted by the close views at: (a) $z/D = 16$, and (b) $z/D = 8$. A general view of the turbulent wake is shown in (c).

In the present investigation, we use the method of snapshots (Sirovich, 1987) and the fluctuating velocity field $\mathbf{u}'$ to decompose the flow at four (x,y)-planes and three (y,z)-planes. A total of 2500 snapshots spanning 100 convective time-units D/U_∞, or equivalently about 22 shedding cycles, were used for this purpose.

In figure 3 we present the energy contribution of each of the first 20 modes in the (x,y)- and (y,z)-slices. In the (x,y)-planes in figure 3(a) the first mode and second mode form pairs and are substantially more energetic than the higher order modes. For the third and fourth modes this pairing is less evident at $z/D = 21$; the energy of modes 3 and 4, in addition, decreases with increasing z, whereas for modes 1 and 2 the energy increases with increasing z. This pattern suggests that at the three upper positions $z/D = 12$, 16 and 21, the flow field is more coherent and dominated by the first and second modes. This loss of coherence with depth is consistent with the gradual inclination of the curved cylinder axis as depth increases (i.e. decreasing z). Axial flows induced by this gradual inclination introduce three-dimensionalities which perturb the flow. In the (y,z)-planes (figure 3.b) the eigenvalues also concentrate most of the energy in modes 1 to 4. In addition, it is possible to notice that the energy in the first mode decreases with increasing streamwise distance.

Tables 1 and 2 show the accumulated contributions to the turbulent kinetic energy for the samples in the (x,y)- and (y,z)-planes, respectively. In table 1 we observe that the first two modes capture between 25% and 50% of the kinetic energy in the flow field at different depths. At the depths of $z/D = 12$, 16 and 21, the vortex shedding is relatively strong to account for more than 40% of the kinetic energy, whereas at $z/D = 8$ the rolling-up of primary vortices is suppressed, leading to a less organized near wake. The energy captured by the first 20 modes varies between 54% at $z/D = 8$, and 65% at $z/D = 21$; thus, the difference in energy captured at different depths is reduced by incorporating more modes. In order to capture 90% of the turbulent kinetic energy at these (x,y)-planes, between 178 and 227 modes would be required; to account for 99% the number of modes required increases to 854. In the (y,z)-planes (table 2) the first and second modes capture less energy compared to the (x,y)-slices; the energy captured decreases with increasing x, as previously commented. This trend is expected since the plane at $x/D = 3$ is closer to the region where the vortices form, which is inherently more organized. As the wake evolves further downstream, it expands and becomes increasingly disorganized, distributing the energy to the higher order modes. Nevertheless, the energy captured with 20 modes, as well as the number of modes to capture 90% and 99% of the energy, are quite similar to the corresponding values for the (x,y)-planes in table 1.

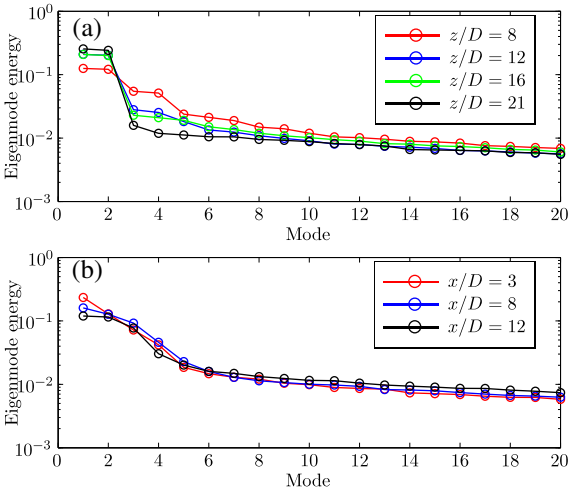

Figure 3. Distribution of the normalized eigenvalues from the POD: (a) (x,y)-slices at different depths z, and (b) (y,z)-slices at different streamwise positions behind the cylinder.

The evolution of the four most energetic temporal coefficients $a_m(t)$ in the (x,y)-planes is shown in figure 4. At $z/D = 8$ the amplitudes of the four modes exhibit a similar order of magnitude, but weak periodicity. At $z/D = 12$ and 16 in figures 4(b) and 4(c), respectively, a_1 and a_2 exhibit a distinct quasi-periodic pattern with larger amplitude than a_3 and a_4. Furthermore, the amplitudes of modes ϕ_3 and ϕ_4 seem to decrease with increasing z. Finally. at $z/D = 21$ (figure 4.d) the first two modes a_1 and a_2 are periodic, while at the same time the traces of periodicity in the third and fourth modes vanish.

Table 1. Contribution of the first two and 20 modes to the turbulent kinetic energy obtained from the POD of the (x,y)-slices. The number of modes needed to capture 90% and 99% of the energy are denoted as $N_{90\%}$ and $N_{99\%}$, respectively.

z/D	$\lambda_1+\lambda_2$	$\sum_{n=1}^{20}\lambda_n$	$N_{90\%}$	$N_{99\%}$
8	24.68%	54.28%	227	825
12	41.12%	60.60%	203	854
16	40.81%	60.83%	192	832
21	49.71%	65.12%	178	822

Table 2. As table 1; POD of the (y,z)-planes.

x/D	$\lambda_1+\lambda_2$	$\sum_{n=1}^{20}\lambda_n$	$N_{90\%}$	$N_{99\%}$
3	36.33%	62.78%	172	824
7	28.76%	58.69%	199	874
12	23.47%	52.13%	203	764

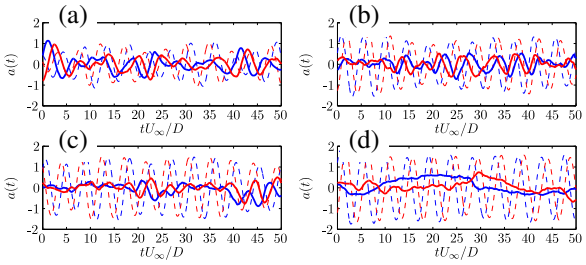

Figure 4. Temporal modes $a_n(t)$ from the POD of the (x,y)-slices; blue dashed line, mode 1; red dashed line, mode 2; blue thick line, mode 3; and red thick line, mode 4. Plots are at the depths: (a) $z/D=8$, (b) $z/D=12$, (c) $z/D=16$, and (d) $z/D=21$.

The degree of dominance of the most energetic temporal mode a_1 over mode a_3 can also be observed in the phase portraits (Lissajous curves) of these modes (figure 5). At $z/D=8$ the orbits exhibit an irregular pattern where neither of the two modes seems to dominate. Decreasing the depth gives rise to a gradual dominance of mode a_1 over a_3, as we see in the orbits at $z/D=12$ and 16. The orbits at $z/D=21$, as figure 5(d) depicts, are clearly dominated by the first temporal mode, suggesting a high degree of coherence at this vertical position. At $z/D=21$ the axis of the cylinder is normal to the free-stream direction, similar to a uniform straight cylinder, and higher coherence is therefore expected in the vortex street.

In order to visualize the spatial distribution of the most energetic modes at each depth, the first ϕ_1 and third ϕ_3 spatial modes corresponding the streamwise velocity fluctuations u' are presented in figures 6(a) and 6(b), respectively. We observe that, irrespective of depth, the first spatial mode ϕ_1 exhibits two anti-symmetric rows. This pattern suggests that two rows of Kármán vortices dominate the flow dynamics. The intensity of mode 1 in figure 6(a) is higher in the first pair of the anti-symmetric row, in consistence with the approximate location of the peak of $\overline{u'u'}$ (see figure 8), known as *vortex formation length* (Williamson, 1996*b*); in this context vortex formation applies only for the planes at $z/D=12$, 16 and 21, as the formation of vortices is suppressed at $z/D=8$. As the depth increases (or correspondingly decreasing z), the free shear layers gradually participate in the mode 1; see for instance the contours of ϕ_1 at $z/D=8$. This shift towards the shear layers could be associated with the increasing degree of instability in the shear layers as the axis of the cylinder becomes more aligned with the streamwise direction.

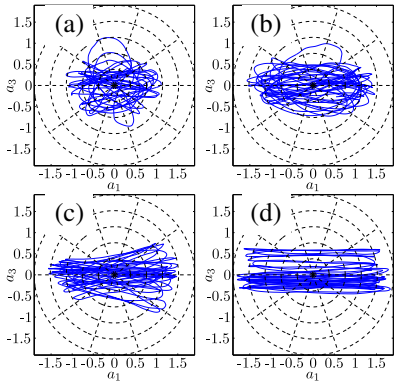

Figure 5. Phase portraits of the modes $a_1(t)$ and $a_3(t)$. Plots are at the depths: (a) $z/D=8$, (b) $z/D=12$, (c) $z/D=16$, and (d) $z/D=21$.

The contours of the spatial mode ϕ_3 shown in figure 6(b) vary greatly with depth. At $z/D=8$ there is a clear dominance of the shear layers with opposite sign compared to ϕ_1 at the same location. Two peaks arise in the vortex formation region at $z/D=12$, also with opposite sign when compared to ϕ_1. At $z/D=16$ there is contribution with the same sign to ϕ_3 from the two shear layers at each side of the cylinder, as well as two regions with opposite sign which arise further downstream. A similar pattern is observed in the contours of ϕ_3 at $z/D=21$ regarding the shear layers, but the pattern downstream in the wake is more diffuse.

Finally, we qualitatively evaluate the capability of the POD for reconstructing the flow field. For this purpose, we use the first 20 modes from the POD to reconstruct the instantaneous turbulent kinetic energy at the first snaptshot. In figure 7(a) we present the original instantaneous kinetic energy, accompanied by the reconstructed fields in figure 7(b). By using 20 modes the main features of the kinetic energy field are reproduced, especially the more intense regions. Although this reconstruction is qualitatively good, small scale features could be represented in the reconstruction by using about 200 modes; i.e. capturing 90% of the turbulent kinetic energy in the reconstruction (see table 1).

Reynolds stresses

In engineering applications the Reynolds number range is considerably higher than the one used in the present case. Risers and other offshore structures, for instance, involve Reynolds numbers of the order of 10^5-10^6. For this reason, the numerical simulation of these industrial flows frequently relies on turbulence closure models. Although the Reynolds number in the present case is at least one order of magnitude lower than that encountered in the most com-

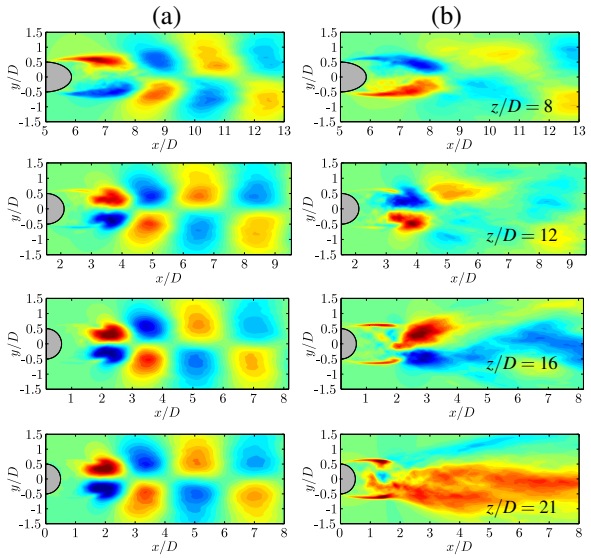

Figure 6. Spatial modes corresponding to the streamwise velocity fluctuations u' at four horizontal (x,y)-slices: (a) mode 1, and (b) mode 3. Negative values are depicted by blue contours, and positive values by red contours.

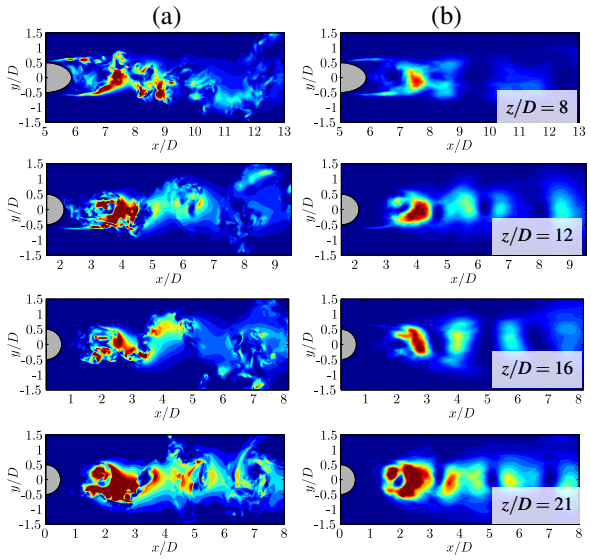

Figure 7. Reconstruction of the instantaneous turbulent kinetic energy in the first snapshot at different (x,y)-slices; 30 contours varying from 0 to 0.3 are plotted. (a) Instantaneous turbulent kinetic energy, and (b) reconstruction using the first 20 modes.

mon industrial applications, knowledge of the influence of the curvature on the Reynolds stresses may complement the selection and validation of turbulence closure models. In the present section we present relevant Reynolds stresses in the wake behind the curved cylinder and discuss their variation with depth.

Figure 8 shows horizontal (x,y)-slices of $\overline{u'u'}$ plotted at four different depths. This Reynolds stress component becomes more intense with decreasing depth (or increasing z); this tendency is likely related to the strength of the vortex shedding at each particular depth. At $z/D = 8$ (only $2D$ above the horizontal extension) the $\overline{u'u'}$-contours are more intense in the free shear layers. This upstream shift in in-

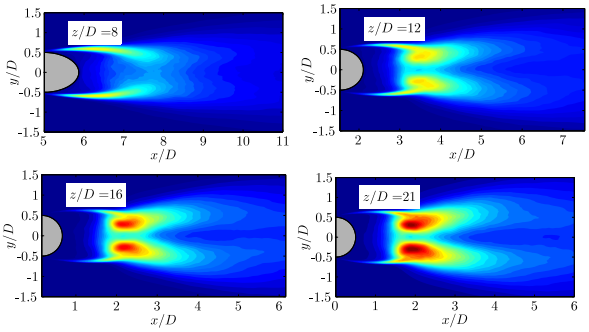

Figure 8. Iso-contours of Reynolds stresses $\overline{u'u'}/U_\infty^2$ at four different depths. Thirty iso-contours in the interval $0 \leq \overline{u'u'} \leq 0.2U_\infty^2$ are considered.

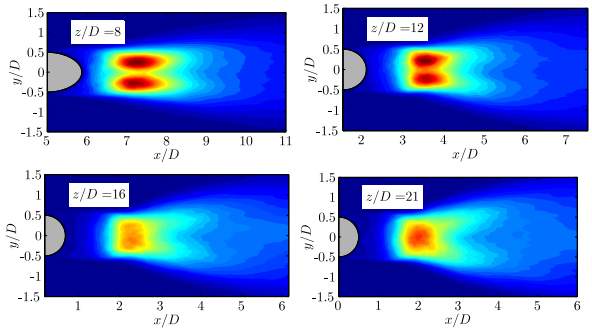

Figure 9. Iso-contours of Reynolds stresses $\overline{w'w'}/U_\infty^2$ at four different depths. Thirty iso-contours in the interval $0 \leq \overline{w'w'} \leq 0.12U_\infty^2$ are considered.

tensity at this vertical position is related to the strong instabilities in the shear layers induced by the curvature of the cylinder, together with the suppression of vortex formation. At $z = 12$, 16 and 21 two distinct spots of high intensity are seen in the contours of $\overline{u'u'}$. This pattern is symmetric with respect to the wake centreline, and a profile of $\overline{u'u'}$ at these depths along the centreline would exhibit two peaks, similar to those observed in previous experiments of the flow past a straight circular cylinder at the same *Re* (Parnaudeau *et al.*, 2008).

Contour plots of $\overline{w'w'}$ at the same depths are shown in figure 9. Two different patterns emerge here. In the upper part of the curved cylinder ($z/D = 21$ and 16) there is one central spot with high $\overline{w'w'}$-intensity. At $z/D = 21$ the flow is almost two-dimensional in the statistical sense, therefore the presence of $\overline{w'w'}$ could be attributed mostly to the vertical velocity fluctuations induced by the vortex shedding. Behind the lower part of the curved cylinder, at $z/D = 12$ and 8, the $\overline{w'w'}$-contours exhibits two peaks instead of one. The intensity at these two peaks is higher than at the peaks in the contours taken at $z/D = 16$ and 21. This evidence suggests that the production of $\overline{w'w'}$ is greatly influenced by the three-dimensional flow that develops in the lee side of the curved cylinder.

Up to this point we have observed a decrease in $\overline{u'u'}$ with decreasing z, together with an increase of $\overline{w'w'}$ with decreasing z; let us now look at the correlation between u' and w' in figure 10. At $z/D = 21$ the magnitude of this Reynolds stress component is very low. This is in accordance with the two peaks of $\overline{u'u'}$ out of the centreline and one central peak of $\overline{w'w'}$, resulting in a very low correlation. The low correlation between u' and w' is also consistent with the quasi-

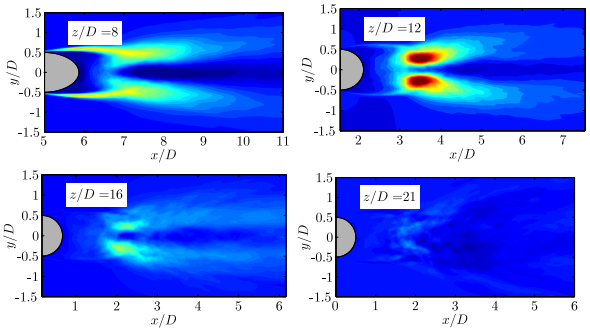

Figure 10. Iso-contours of Reynolds stresses $\overline{u'w'}/U_\infty^2$ at four different depths. Thirty iso-contours in the interval $-0.006U_\infty^2 \leq \overline{u'w'} \leq 0.04U_\infty^2$ are considered.

two-dimensionality of the wake at this vertical position. At $z/D = 16$ the correlation between u' and w' increases somewhat, despite having the same pattern of $\overline{u'u'}$ and $\overline{w'w'}$ as at $z/D = 21$. The highest intensity in $\overline{u'w'}$ occurs at $z/D = 12$, with two symmetric peaks. At $z/D = 8$ the intensity in the peaks of $\overline{u'w'}$ decreases and their location shifts upstream towards the free shear layers. This evidence suggest that the highest intensity in $\overline{u'w'}$ is achieved as a combination of vortex formation strength and axial flow induced by the curved axis.

CONCLUDING REMARKS

In the present paper we have reported results from a DNS of the wake behind a curved circular cylinder. We focused our analysis on the instantaneous wake topology, the POD decomposition of the flow field, and the time-averaged Reynolds stresses.

Despite the high complexity of the instantaneous vortical structures, the dynamics of the flow past this curved cylinder configuration seem to be dominated by the rolling-up of the shear layers, and eventual formation and shedding of Kármán vortices. In the lower part of the cylinder, the gradual alignment of the cylinder axis with the free-stream direction has an impact on the coherence of the wake. Small vortical structures characteristic of the turbulence propagates in a disorganized way in the lower part of the curved cylinder, whereas in the upper part the small structures are periodically convected by the primary vortices.

We also conducted a POD analysis to extract the dominant coherent modes at different locations in the wake. From this analysis we found that the two most energetic modes capture between 25% and 50% of the turbulent kinetic energy at the depths sampled. The dominance of the first two modes in the POD was related to the strength of the vortex shedding at each particular depth. At $z/D = 8$, the lower energy of the first two modes confirms that the wake behind the lower part of the curved cylinder is less coherent. In order to represent 90% of the kinetic energy, about 200 modes are needed, making the present case suitable for a low dimensional representation. This is supported by the reconstruction of the instantaneous turbulent kinetic energy with 20 modes, which turned out to capture most of the dominant features in the flow field.

Concerning the Reynolds stresses, it was found that the $\overline{u'u'}$ intensity decreases with depth, whereas the intensity of $\overline{w'w'}$ increases with depth. This dependence on depth is most likely associated with the decreasing strength of the vortex shedding with depth, affecting thereby the fluctuations of the streamwise velocity u'. Additionally, the three-dimensional flow induced by the axial curvature of the cylinder increases the levels of vertical velocity fluctuations w'. Due to the combination of shedding strength and axial flow, the off-diagonal component $\overline{u'w'}$ was highest at an intermediate depth of $z/D = 12$.

ACKNOWLEDGEMENT

This work has received support from the Research Council of Norway (Program for Supercomputing) through a grant of computing time.

REFERENCES

Berkooz, G., Holmes, P. & Lumley, J. L. 1993 The proper orthogonal decomposition in the analysis of turbulent flows. *Annu. Rev. Fluid Mech.* **25**, 539–575.

De Vecchi, A., Sherwin, S. J. & Graham, J. M. R. 2009 Wake dynamics past a curved body of circular cross-section under forced cross-flow vibration. *J. Fluids Struct.* **25**, 721–730.

Frederich, O. & Thiele, F. 2011 Turbulent flow dynamics caused by a truncated cylinder. *Int. J. Heat Fluid Fl.* **32**, 546–557.

Jeong, J. & Hussain, F. 1995 On the identification of a vortex. *J. Fluid Mech.* **285**, 69–94.

Manhart, M. 2004 A zonal grid algorithm for DNS of turbulent boundary layers. *Comput. Fluids* **33**, 435–461.

Miliou, A., De Vecchi, A., Sherwin, S. J. & Graham, J. M. R. 2007 Wake dynamics of external flow past a curved circular cylinder with the free stream aligned with the plane of curvature. *J. Fluid Mech.* **592**, 89–115.

Narasimhamurthy, V. D., Andersson, H. I. & Pettersen, B. 2009 Cellular vortex shedding behind a tapered circular cylinder. *Phys. Fluids* **21**, 044106.

Parnaudeau, P., Carlier, J., Heitz, D. & Lamballais, E. 2008 Experimental and numerical studies of the flow over a circular cylinder at Reynolds number 3900. *Phys. Fluids* **20**, 085101–085101.

Peller, N., Le Duc, A., Tremblay, F. & Manhart, M. 2006 High-order stable interpolations for immersed boundary methods. *Int. J. Numer. Meth. Fl.* **52**, 1175–1193.

Ramberg, S. E. 1983 The effects of yaw and finite length upon the vortex wakes of stationary and vibrating circular cylinders. *J. Fluid Mech.* **128**, 81–107.

Sirovich, L. 1987 Turbulence and the dynamics of coherent structures. *Quart. Appl. Math.* **45**, 561–590.

Williamson, C. H. K. 1996*a* Three-dimensional wake transition. *J. Fluid Mech.* **328**, 345–407.

Williamson, C. H. K. 1996*b* Vortex dynamics in the cylinder wake. *Annu. Rev. Fluid. Mech* **28**, 477–539.

Zhou, T., Wang, H., Razali, S. F. M., Zhou, Y. & Cheng, L. 2010 Three-dimensional vorticity measurements in the wake of a yawed circular cylinder. *Phys. Fluids* **22**, 015108.